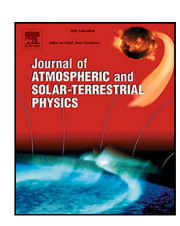


Contents lists available at ScienceDirect

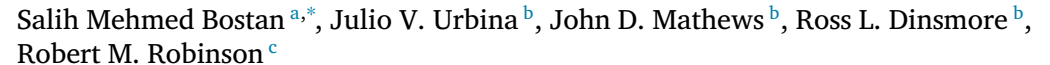
Journal of Atmospheric and Solar–Terrestrial Physics

journal homepage: www.elsevier.com/locate/jastp



Research paper

Multi-instrument study of a spread-F event at Arecibo linked to solar wind variations



- ^a Bursa Technical University, Department of Electrical and Electronics Engineering, Mimar Sinan Campus, Yildirim, Bursa, 16310, Turkey
- b The Pennsylvania State University, Department of Electrical Engineering, 121 Electrical Engineering East, University Park, 16802, PA, USA
- ^c Catholic University of America, Washington, DC, USA

ARTICLE INFO

Keywords: Mid-latitude spread-F Ionospheric irregularities Solar wind pressure pulses GNSS delta-vTEC keograms

ABSTRACT

Using five diverse data sets, we demonstrate that apparently local ionospheric spread-F activity, observed with an HF radar and the Arecibo Observatory (AO) Incoherent Scatter Radars (ISR) under geomagnetically quiet conditions, is likely the local manifestation of a mesoscale or larger ionospheric response to relatively weak solar wind activity. The solar wind activity included a weak pressure pulse and Interplanetary Magnetic Field (IMF) realignment events. The mid-latitude spread-F activity was observed with a 4.42 MHz radar located near AO and the dual-beam 430 MHz AO ISRs. Additionally, the Coupling, Energetics and Dynamics of Atmospheric Regions (CEDAR) Madrigal Global Navigation Satellite System-Total Electron Content (GNSS-TEC), the NASA OMNI, and the SuperMAG datasets were used to establish the (mesoscale/global) wide-context of the local, deep-context radar results. While the ISR event appears to be "classical" local spread-F, often attributed to Perkins-like plasma instabilities, the HF radar reveals large ionospheric structures coincident with the ISR event. However, that the apparently AO-local event was part of a very dynamic mesoscale event that lasted for over ten hours, is shown via independent AO-sector and AO-conjugate sector keograms constructed using detrended vertical TEC (delta-vTEC) data. The keograms reveal a prominent F-region feature that appears to propagate from west-to-east and then back to the west passing over AO twice. The ISR manifestation of this mesoscale event is indistinguishable from decades of similar ISR results which were assumed to be strictly "local". The strong non-local (mesoscale) properties revealed by the delta-vTEC keograms suggest a possible space weather influence. Study of the relevant NASA OMNI solar wind and superMAG magnetometer data points to modest solar wind features including IMF realignment that may have electrodynamically launched, with little time delay, the observed mesoscale ionospheric events. Given the apparent rapid ionospheric response to the solar wind features, we suggest that limited latitudinal scale, prompt penetration electric fields (PPEF), associated with highly-localized partial ring current activity, be considered in the system-of-systems context of our observations. In any case, the need to examine magnetospheric/ionospheric electrodynamics across a wide range of instruments and data sets is demonstrated.

1. Introduction

We describe rather surprising Arecibo Observatory (AO) incoherent scatter and HF radar observations of the ionospheric phenomenon widely known as "spread-F". These unique observations were conducted over \sim 12.5 h beginning at 22:41 AST (Atlantic Standard Time = UT-4 h) 14 March 2017 and ending at about 11:00 h 15 March 2017. This was a geomagnetically quiet period near solar minimum and so spread-F activity was expected and observed. As we had recently developed the open-source software needed to ingest and analyze GNSS-TEC

(Global Navigation Space System – Total Electron Content; Dinsmore et al., 2021a,b), we examined relevant data processed to keogram (defined later) form revealing that the AO-local spread-F was part of a mesoscale structure that was also observed in the AO-conjugate keogram. Taken as a whole, these radar and keogram results suggest a link to solar wind properties as revealed in the OMNI and superMAG data. We first provide a brief history of spread-F studies which is then followed by an in-depth description of our results and conclusions.

E-mail addresses: salih.bostan@btu.edu.tr (S.M. Bostan), jvu1@psu.edu (J.V. Urbina), jdm9@psu.edu (J.D. Mathews), rld5204@psu.edu (R.L. Dinsmore), robinsonr@cua.edu (R.M. Robinson).

^{*} Corresponding author.

The ionospheric phenomenon known as spread-F has been under investigation for nearly a century following detection with early swept-frequency HF radars - ionosondes (ionospheric sounders) - as described by Berkner and Wells (1934) and Booker and Wells (1938). Spread-F as seen on ionograms is the splitting and/or spreading in virtual range and frequency of the ordinary (O) and extraordinary (X) traces from F-region virtual ranges. Ionograms exhibiting spread-F and relevant to this discussion are given as Fig. A.1 in the ancillary section. Booker (1961) provided essential insight in his radio science assessment of the complex ionogram traces associated with Vanguard II rocket launch from Cape Canaveral. The rocket plume created an ionospheric depletion tube through the F-region plausibly explaining the ionosonde results. Booker extended this insight to spread-F and radio star scintillation per his Fig. 6 which graphically depicts an entire 3D complex of plasma-depletion tubes. Herman (1966), in a delightful magnum opus, reviewed the observational evidence from all available instruments regarding ionospheric processes leading to ionogram spread-F. He convincingly linked F-region geomagnetic field-aligned irregularities (FAI) to spread-F at all latitudes. Herman also concluded that the perpendicular-B FAI scale was ~1 km with significant parallel-B elongations. Spread-F producing ionospheric structure, comprised of horizontally extended regions of FAI structures (Fig. 6; Booker, 1961), was found to be mesoscale in size. For (Herman, 1966), the question of how mid-latitude FAI structures were created remained open although plasma instabilities were suspect. In his celebrated paper, Perkins (1973) offered what remains, after some caveats regarding instability growth rates and a few other details, the accepted explanation for the observed ~1 km-scale FAI structures and perhaps for the surrounding ~10-100 km scale F-region structure as well. Using the original Arecibo Observatory (AO) 430 MHz Incoherent Scatter Radar (ISR; Mathews, 2013b), Mathews and Harper (1972) associated multi-trace spread-F ionograms with complex vertical and horizontal structure of the nighttime F-region. Although, due mostly to insufficient computer power, the time and range resolution was insufficient to resolve ionospheric structure below ${\sim}10$ km, the F-region structure reported by Mathews and Harper (1972) was likely what we now refer to as "upwelling". These observations were continued by Behnke (1979) who used the AO ISR beam-swinging mode to discover and track the passage of F-region high/low altitude "bands" or "slabs", at times up to 70 km in height and no more than 10 km in thickness.

Since these early reports, the morphology, occurrence rate, and origins of spread-F have been the subject of a great deal of research employing radio science tools such as ionosondes (Bowman, 1990) and coherent scatter and incoherent scatter radars (e.g., Swartz et al., 2000; Mathews et al., 2001a; Hysell et al., 2018) along with theoretical analyses as described in Ossakow (1981), Bowman (1990), Swartz et al. (2000), Zhou et al. (2006) and Hysell et al. (2018) among others. As mentioned above, the term spread-F was coined in the early days of ionospheric research when the ionosonde and other HF radars were the principal instruments. As ionosonde technology and distribution expanded, the definition of spread-F grew to include diffuse echoes that were assumed to be due to scattering, as opposed to reflection, from small-scale plasma instability structures and other sounder wavelength scale structures including FAI in the region where the radar illuminates the radar wave vector (\vec{k}) perpendicular to the geomagnetic field (\vec{B}) or $\vec{k} \perp \vec{B}$ region of the ionosphere. Different ionogram classifications have included both resolved and unresolved spread-F and range and frequency spread-F along with equatorial, midlatitude, and high-latitude spread-F. Importantly the term has been carried over to pronounced F-region ionospheric structures such as a strong upwelling with kilometer-scale substructure as detected by the 50 MHz MU radar in coherent scattering and by the AO ISR. The definition used herein is in reference to Figs. 1 & 2 of Mathews et al. (2001a), Fig. 2 in Mathews et al. (2001b), Fig. 8 in Seker et al. (2007), and Figs. 1 & 2 in Hysell et al. (2018). Additionally, equatorial spread-F (ESpF) plumes, also of possible concern expressed herein, have long

been featured in studies conducted at the Jicamarca Radio Observatory. e.g. Woodman (2009) and Hysell et al. (2018). High latitude spread-F (HLSpF) and its origins are reviewed in Keskinen and Ossakow (1983). As noted by Hysell et al. (2018), ESpF and HLSpF are each attributable to the respective instabilities inherent to the horizontal geomagnetic field unstably supporting the ionosphere against gravity (Woodman, 2009) while HLSpF is a direct consequence of the near vertical polar geomagnetic field and the resultant efficient magnetospheric-ionospheric (MI) coupling with inherent plasma instabilities (Keskinen and Ossakow, 1983). At middle latitudes, with geomagnetic field lines neither horizontal nor vertical, the origins of mid-latitude spread-F (MLSpF) are perhaps less clear. Into the 1950s the MLSpF generative process was unknown but that, observationally, it was suppressed during the day. The overall process was explained by Perkins (1973). That is, that the daytime plasma concentration profiles are governed by ionization and recombination mechanisms which are rapid compared to ionospheric convection which in turn prevents convective motions from modulating the Pedersen conductance, a condition that must be met for the MLSpF instability to develop and grow. Simply put, the daytime photochemical E/F1-region electrically shorts the highly conducting F-region flux tubes stabilizing the F-region while, conversely, the nighttime E-region valley electrically opens the highly conducting F-region flux tubes allowing E fields to develop. A more comprehensive description of the Perkins mechanism is given in the introduction of Mathews et al. (2001b). Fuller descriptions are given in Kelley (2009), Chapter 6, Zhou et al. (2006), and Perkins (1973).

Modeling studies indicate that the Perkins mechanism alone has a slow growth rate that cannot quickly produce the observed spread-F structures without sufficient "seeding" (pre-conditioning) perturbation structures (Kelley and Fukao, 1991). That is, plasma structures of appropriate scale and amplitude to initiate bottom-side F-region Perkins instabilities that grow to the observed characteristics over a few hours at most are needed. Based on MU radar observations of spread-F structures (Fukao et al., 1991) and Kelley and Fukao (1991) proposed that acoustic-gravity wave (AGW) modulation of the atmosphere/ionosphere at F-region altitudes were a likely seed mechanism. Miller et al. (1997) also argue that AGWs induce Perkins-like plasma instabilities in the night-time ionosphere over Arecibo Observatory. While recognizing that AGWs are likely an important mechanism seeding the mid-latitude Perkins instability, we report multi-instrument observations that suggest that solar wind IMF and pressure features may have a role even at low solar activity levels. To our knowledge this regime has not been previously explored.

In this paper we present unique, multi-instrument observational evidence for a non-local – mesoscale to possibly global – ionospheric electrodynamic event that manifests at AO as mid-latitude spread-F. Using the evidence provided from five independent sources, we introduce the possibility that solar wind variations provide an additional spread-F seeding mechanism, which will be discussed in the rest of the paper. The event was locally (deep-context) observed at AO by both a low power 4.42 MHz HF radar and the dual-beam 430 MHz ISRs. The near solar minimum, low geomagnetic activity, nighttime radar spread-F activity is herein identified as a feature within an AOsector mesoscale ionospheric structure observed via (keogram) analysis of GNSS TEC. The radar and TEC F-region structures are ultimately linked to a relatively minor space weather event that spanned the radar observation period and includes a solar wind pressure pulse as well solar wind as three magnetic field (IMF) realignment events (e.g., Huang, 2020). Given the apparent rapid ionospheric response to these modest solar wind features, we suggest that limited latitudinal scale, prompt penetration electric fields (PPEF), associated with highlylocalized partial ring current activity (e.g., Fukushima and Kamide, 1973; Tsurutani et al., 2004, 2008), be considered in the system-ofsystems context of our observations. We present our results over four main sections. Following the Introduction, we first briefly describe the data acquisition systems and resultant data sets. We then present the core results and integrate them into a coherent whole. Finally, we discuss the results with concluding remarks.

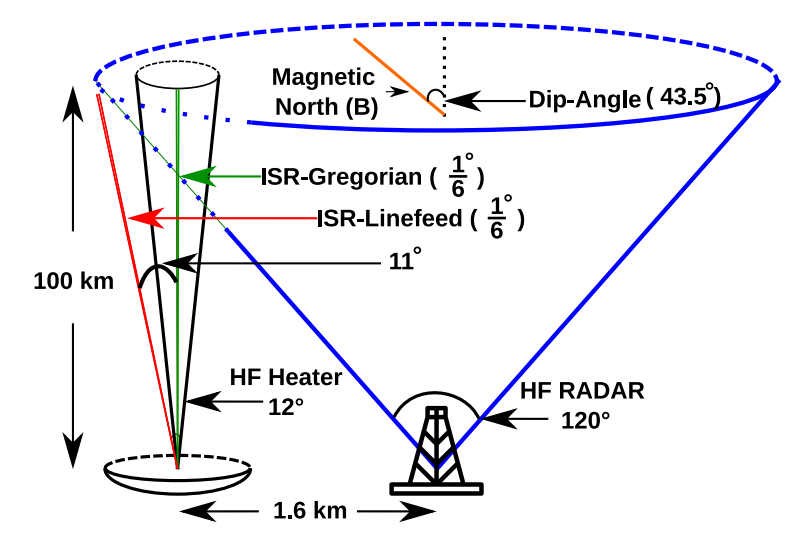


Fig. 1. Schematic (not to scale) representation of the geometry of Arecibo Observatory (AO) HF heater, HF radar, and 430 MHz incoherent scatter radar (ISR). The elevation plane of the HF antenna is 120.1° at $\phi = 0^{\circ}$, 101° at $\phi = 45^{\circ}$, and 80° at $\phi = 90^{\circ}$.

2. Instrumentation

Multiple instruments and data sets were used to observe and trace the unusual MLSpF structure reported herein. Each instrument is described in the following subsections. These include the 4.42 MHz Penn State Ionospheric Radar Imager (PIRI) radar, Arecibo HF heater, the dual-beam 430 MHz AO ISR, and the appropriate GNSS-TEC receiver array. A sketch of the geometry of the observations with respect to the radars is in Fig. 1. The PIRI HF radar was deployed near a HAM radio station close to the observatory. The GNSS-TEC receivers are located across the Caribbean island chain and across South America. The OMNI data set is primarily data from satellites at L1 and the SuperMAG data set is gathered from a global network of magnetometers.

2.1. PIRI HF (4.42 MHz) radar

PIRI, is a software-defined HF radar which was designed and implemented as described by Bostan et al. (2019) to study ionospheric plasma instabilities. In early March 2017, PIRI was deployed near AO (18.36° N, 66.75° W, 43.5° dip-angle, radar frequency = 4.42 MHz) in order to utilize the AO ionospheric heater system during an HF heating campaign. The HF radar setup was identical to the system described in Bostan et al. (2019) except for its operating frequency and transmit front end. An inverted-V type dipole antenna centered at $f_0 = 4.42$ MHz was used for transmitting. The voltage standing-wave ratio of the antenna was less than 1.2 over a 50-kHz bandwidth. Half-power beamwidth of the antenna in the elevation plane is 120.1° at $\phi = 0^{\circ}$ as shown in Fig. 1, 101° at $\phi = 45^{\circ}$, and 80° at $\phi = 90^{\circ}$. The transmitting antenna beam points at zenith and it is horizontally polarized. An HF linear tube ham radio amplifier, Ameritron AL-811H, is used in the final stage of the amplification and was able to provide 625 W peak power even though it is used slightly off its operating region. At the receiver front end, PIRI used two wide-band horizontal crossed-dipole active antennas for reception allowing circular polarization analysis. A more comprehensive description of the system and its components can be found in Bostan (2018) and Seal (2012, 2017). Several signal processing techniques are applied to the HF data including zero sidelobe decoding of the Barker codes, filtering the DC offset and filtering interference. Sidelobes of the decoded Barker sequence can adversely impact interpretation of radar data particularly in a high dynamic range environment. Thus, a sidelobe-free decoding filter is applied based on Lehtinen et al. (2004) and Kesaraju et al. (2017). During the March 2017 heating campaign, the PIRI HF radar was deployed to run a set of D-region wave interaction (cross-modulation) experiments (e.g., Sulzer

et al., 1982). The data set presented herein was recorded in an attempt at wave interaction. However, the 5.125 MHz heater interference due to arcing has proven insurmountable. Fortunately, we are nonetheless able to thoroughly document the extended spread-F activity revealed in this, especially now that AO is deceased, unique dataset. The AO HF heater was operating during some intervals within the observing period and was prone to arcing thus generating strong wideband interference. This interference tended to saturate the wideband amplifier of the active receive antennas. As indicated in Table 1, the HF heater was operating in a pulsed mode starting from midnight until 07:30 LT. Those individual PIRI pulse returns exhibiting heater arcing interference were removed from the HF range-time intensity (RTI) plots which resulted in the elimination of almost half of the radar pulses.

2.2. Arecibo 430 MHz incoherent scatter radar

The Arecibo Observatory 430 MHz incoherent scatter radar (ISR, in single and, ultimately, dual-beam mode) had been in operation since 1963 through to a few months before the untimely demise of the telescope on 1 December 2020. A history of ISR at AO is given in Mathews (2013a,b). Famously and fortunately, the 305 m spherical cap dish, as conceived by William Gordon, was far bigger than needed for basic ionospheric probing. This was due to assumptions regarding the spectral width of the ionospheric radar signal. The operational 430 MHz ISR was 20-80 times, depending on mode of operation, more sensitive than other ISRs. Incoherent scattering is extensively reviewed in the literature, e.g., Evans (1972) and Mathews (1986). The AO ISR has a 1/6 degree pencil beam and, via the theory of incoherent scattering, parameters such as electron concentration, wind velocity, ion-neutral collision frequency can be inferred (Mathews, 1984). In the observations presented here, both the linefeed and Gregorian systems were used. For these observations, as shown in Fig. 1, the Gregorian was pointing at zenith while the linefeed was pointed 11° magnetic south.

2.3. GNSS delta-vTEC

The third and final "instrument" used in this study is the GNSS-TEC receiver network. The GNSS-TEC receiver network covers much of the non-oceanic latitudes and longitudes and can provide a global (wide context), distributed image of ionospheric F-region electron total electron content — peak electron concentration is taken to be at 350 km altitude. The geographical location of each 30 s TEC measurement is the point at which the receiver-satellite line-of-sight passes through 350

km altitude. The GNSS-TEC receiver network provides the GNSS-TEC data set, which is available from the CEDAR (Coupling, Energetics and Dynamics of Atmospheric Regions) Madrigal database (http://cedar. openmadrigal.org/) with additional TEC data made available from the LISN (Low Latitude Ionospheric Sensor Network) network (http: //lisn.igp.gob.pe). The GNSS-TEC data set consists of electron column concentration measurements (in TECU units, $10^{16} \frac{el}{m^2}$) that are derived from the propagation delays introduced by electrons in the path of the GNSS signal to the receiver on the ground (e.g., Coster et al., 1990, 1992). That initial line-of-sight column electron concentration (called slant-TEC, or sTEC) is mapped to a vertical path to yield vertical-TEC (vTEC) (Rideout and Coster, 2006; Vierinen et al., 2016). The opensource software GRITI (available per Dinsmore, 2021) is then used to detrend the vTEC data to produce the delta-vTEC data set used for analysis herein (Dinsmore et al., 2021b). The delta-vTEC data set provides millions of measurements of perturbations in the ionosphere, along with associated latitude, longitude, and timestamps. The noise amplitude associated with sTEC measurements is very low (0.02 TECU) compared to expected amplitudes (~0.5 TECU; Coster et al., 2013). Additionally, the process that maps sTEC to vTEC suppresses noise farther by reducing the amplitudes of (relatively) noisier low elevation angle measurements.

Dinsmore et al. (2021a) introduces the keogram analysis method (see Figs. 4 and 5 herein) which, in our application, reduces a visually challenging movie of delta-vTEC versus latitude/longitude versus time to a static figure showing delta-vTEC versus longitude versus time where all data in each longitude-narrow/latitude-wide "pixel" is averaged per Fig. 4 template. This averaging approach yields results that are very resistant to systemic noise from GNSS constellation sampling issues and associated biases even at low measurement densities. The delta-vTEC keogram analysis method was introduced by Dinsmore et al. (2021b). The code is available within the open-source software GRITI (https://github.com/dinsmoro/GRITI).

A more detailed description of the keogram approach as a robust analysis method for delta-vTEC data is given in Dinsmore et al. (2021a). The keogram analysis method is based on the concept introduced by Eather et al. (1976) which has been extended to apply to TEC products. It primarily consists of slicing (pixilating) a geographic area into strips, in this case latitude-wide and longitude-thin strips (vertical strips in our visualizations; see Fig. 4) and averaging the data in each pixel over a specified time interval. That is, all delta-vTEC points within a single strip are averaged together to produce a single pixel for each time interval, 30 s in these results. Each 30 s cadence row of pixels is displayed on the ordinate for each time interval (abscissa) creating a static "movie" of the progression of delta-vTEC activity through time—the keogram. Fig. 4 shows the keogram averaging framework (slicing template) for AO-, AO-conjugate-, and SA-sectors that yields the respective keograms in Fig. 5. For the keogram averaging-templates given in Fig. 4, the vertical magenta lines represent the slicing direction applied to the mapped geographic area. Importantly, the slices shown here are a reduced number of slices for visualization purposes - the actual slices are 10 times denser. The scattered data points in Fig. 4 are a 30 s realization (at 0:00:00 UT 14 March 2017; -28 h in Fig. 5) of all satellite-receiver line-of-sight 350 km altitude pierce points color coded to delta-vTEC values per the color bar. All the satellite pierce point delta-vTEC values within each slice (pixel) at each 30 s interval are averaged to one number which represents that delta-vTEC pixel value at that time for the slice central longitude. This process is repeated for all timestamps to yield a cohesive view of longitudinally-moving deltavTEC activity in the form of the keograms in Fig. 5. The upper left keogram averaging-framework (a) has 50 slices and each slice is 0.32 arcdegrees (approximately 36 km) wide in longitude and 16 arcdeg tall in latitude. The upper right keogram averaging-framework (b) has 50 slices that are 0.5 arcdeg (approximately 55 km) wide in longitude and 25 arcdeg tall in latitude. The lower keogram averaging-framework

(c) has 50 slices that are 0.94 arcdeg (approximately 104 km) wide in longitude and 25 arcdeg tall in latitude.

NOTE: AO is located at $18.3464^\circ N$ and $293.2472^\circ E$ ($-66.7528^\circ E$). The 2017 AO 350 km altitude geomagnetic conjugate point is located near $35.88^\circ S$ ($\pm 1^\circ$) and $303.21^\circ E$ ($-56.79^\circ E$) ($\pm 1^\circ$) per IGRF13 and using ray tracing. The longitude-band slicing orientation used herein highlights activity that moves perpendicular to the slices (in longitude). For reference, Dinsmore et al. (2021a) shows a simulated propagating feature moving perpendicular to the slices of a keogram averaging-framework.

2.4. SuperMAG and OMNI dataset

Geophysical magnetometers have long been used to measure specific parameters related to the Earth's magnetic field such as its strength, direction, and dynamic properties. They have proven to be an important tool to comprehensively understand magnetosphere-ionospheresolar wind physics (e.g., Gjerloev, 2009). Under the supervision of national organizations, hundreds of magnetometers are currently scattered around the world for various scientific purposes. Geomagnetic activity indices such as Kp have long been used. However, the Super-MAG initiative (Gierloev, 2009) with more modern indices based on 1 min cadence data from a few hundred magnetometers is used for this work (Fig. 6, panel b). More information regarding SuperMAG data is given by Gjerloev (2009) and at the webpage (SuperMAG, 2022). Under the SuperMAG Indices tab near-Earth solar-wind parameters are available from NASA's OMNI database. Also available is data from individual magnetometers such as San Juan and Huancayo. We employ both SuperMAG and OMNI datasets in Fig. 6 in order to better understand the global context surrounding the mid-latitude spread-F event that was detected by PIRI radar, AO ISR, and the delta-vTEC data as presented in keogram form.

3. Results

The MLSpF event results from the PIRI HF radar, AO ISRs, and GNSS delta-vTEC measurements are given in Fig. 2, Fig. 3. and Fig. 5 respectively. In Fig. 2, the peak of the ISR-defined ionospheric upwelling event (Fig. 3) occurs at 03:30 LT. The right-hand red box in this figure and Fig. 3 delineate this signature event. The diffuse, range-spread F-region signature suggests the strong role of HF propagation from offvertical and that overdense scattering (Mathews, 2004) from numerous small-scale F-region structures dominate. The lack of ionospheric returns between 04:00 LT and 07:00 LT indicates that the peak plasma frequency (foF2) dropped below the 4.42 MHz radar frequency. The F-region sunrise at ~07:00 LT with the rapid generation of the photochemical ionosphere is seen in the appearance of the solid O/X-mode traces. Together, Figs. 2 and 3 results leverage more interpretation than either result alone. Throughout this paper, the red boxes enclose the same signature events — the ISR-observed upwelling (right) and solar wind event (left). The pronounced upwelling event at 03:30 LT in Fig. 3 attracted our attention as the corresponding feature in Fig. 2 seems to indicate a much larger horizontal scale event than we had anticipated. This type of low geomagnetic activity nighttime F-region upwelling event has long been assumed to be caused by local Perkins instability and referred to as mid-latitude spread-F. Thus, comparison of both narrow-beam ISR and wide-beam HF radar suggested that the MLSpF event could be possibly a mesoscale event instead of a local Perkins-like instability. This led to the investigation of the GNSS deltavTEC measurements over the Carribean region, Equatorial region, and the magnetic conjugate region of AO. The Fig. 5 GNSS delta-vTEC data are given in keogram form as described in Section 2.3. The averaging framework for the three regions is given in Fig. 4. Note that the three-day keogram time interval supplies additional context for interpretation. The keogram signature of the net MLSpF-like event period in Fig. 5a is the AO- Λ that occurs over -4 and 7 AST. The structure in the

Table 1Active instrument configuration at Arecibo Observatory^a.

	Frequency	IPP	Pulse compression	Range resolution	Pulse width	Peak power
HF Radar	4.42 MHz	6 ms	Barker-13	2.25 km	195 μs	600 W
HF Heater ^b	5.125 MHz	12 ms	None	N/A	1 ms	300 kW
Arecibo ISR	430 MHz	10 ms	Coded Long Pulse	150 m	440 μs	430 kW

^aDetails of other systems that are included in this paper such as GNSS delta-vTEC, SuperMAG, and OMNI data sets are given in Section 2.4. ^bConfiguration is given only for observational context.

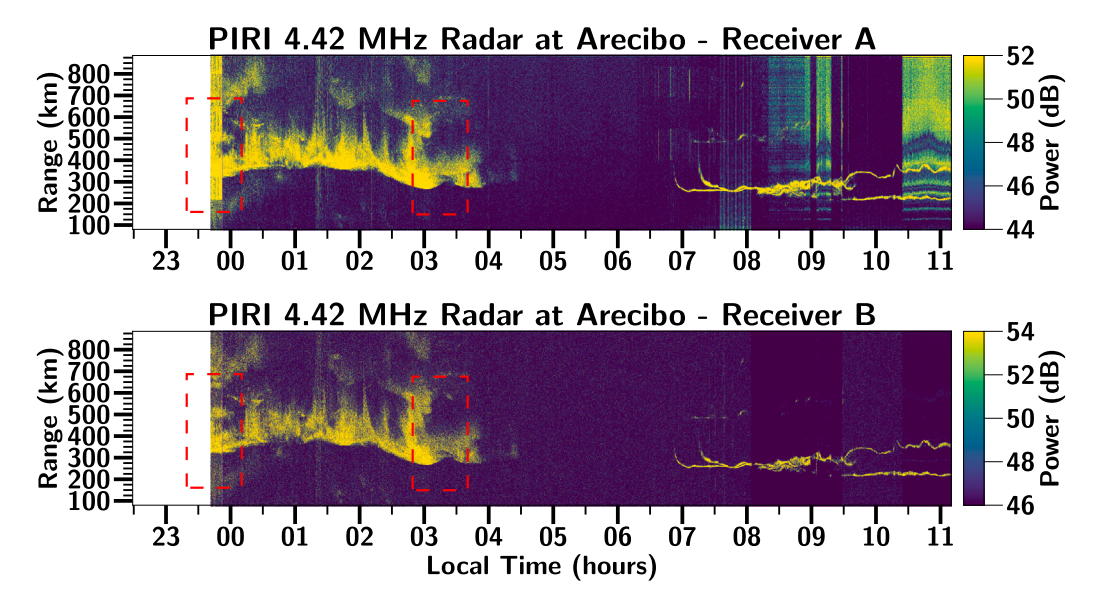


Fig. 2. Apparent mid-latitude spread-F (MLSpF) events captured by the PIRI HF radar. Range-spread MLSpF activity is observed over the 23:41 to ~04:00 LT interval on 15 March 2017. Note that as desribed in Section 2.1, "heater-on" PIRI pulse-returns have been removed due to strong arcing interference and the vertical bars that are visible after 07:30 LT is interference from a continuous wave heating experiment which cannot be removed. Displayed total power in the two orthogonal channels has been adjusted relative to the individual noise levels. The Barker codes are decoded by sidelobe-free decoding algorithm (Kesaraju et al., 2017). Note: Throughout this paper, the red boxes enclose the same signature events.

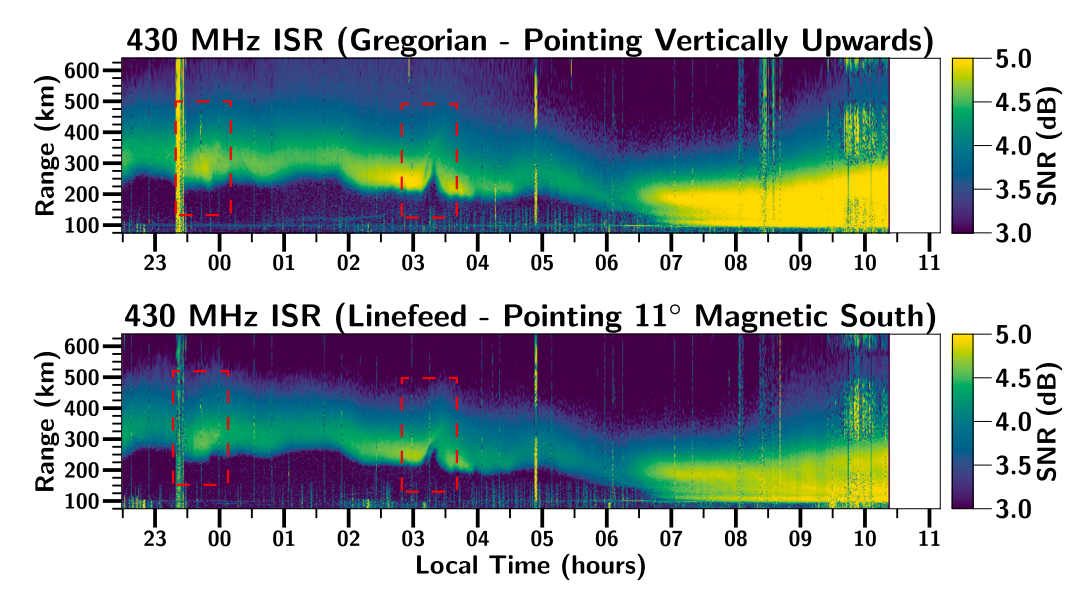


Fig. 3. Dual-beam Incoherent Scatter Radar (ISR) Range-Time-SNR(dB) observational results approximately coinciding with Fig. 2 HF radar observations from 15 March 2017.

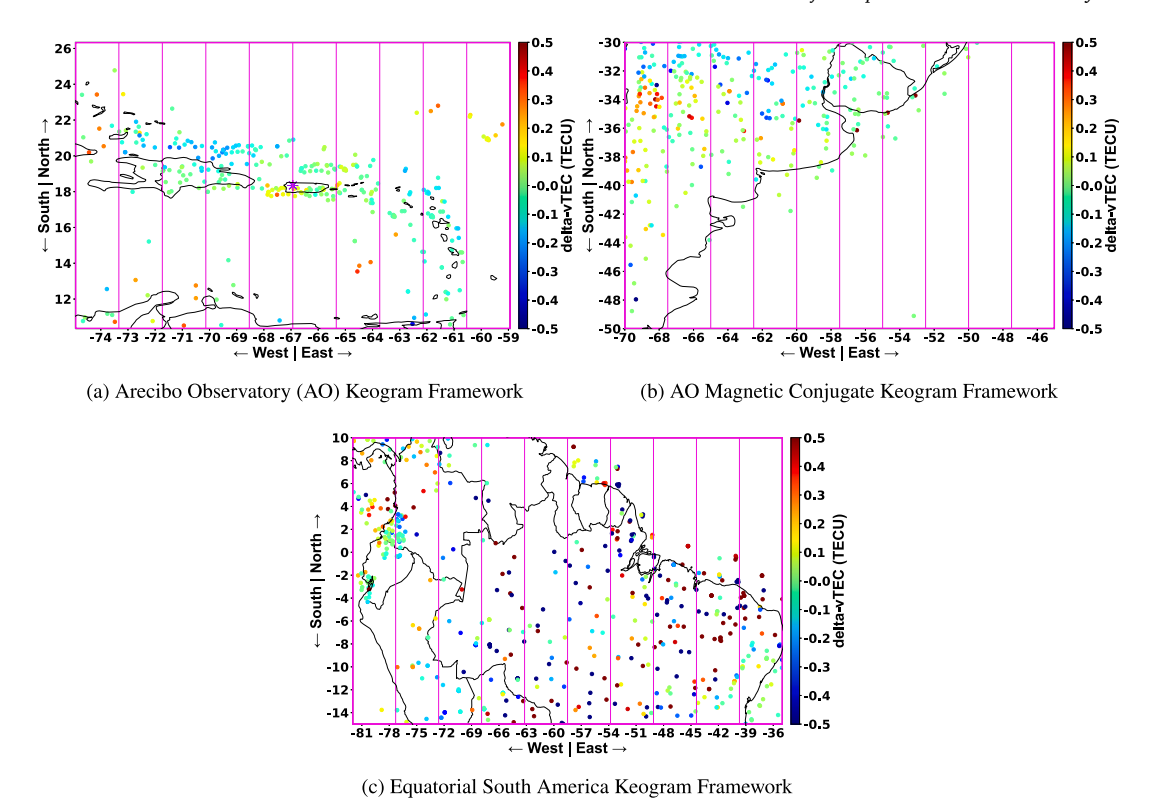


Fig. 4. Keogram averaging-framework for (a) AO and surrounding islands (AO marked with a purple asterisk), (b) magnetic conjugate point of AO, and (c) equatorial South America.

figure is referred to as AO- Λ throughout the paper to avoid confusion as "inverted-V" is used to describe another feature in space physics. The black arrows indicate the central times of Figs. 2 and 3 boxes. The upwelling event time is indicated by the right-hand arrow. The Fig. 5b delta-vTEC keogram (using Fig. 4b averaging framework) for the AO-conjugate region of South America also shows the AO- Λ structure (visible over –4 to 7 h AST) demonstrating the electrodynamic coupling between the nighttime F-regions. Using Fig. 4c averaging-framework, delta-vTEC keogram for magnetic equatorial SA is generated and is given in Fig. 5c. During local nighttime ESpF (Kudeki et al., 2007) activity is readily visible each night. Note that the time and day/night scales for Fig. 5 all correspond to AO. Thus the blue sunrise/set demarcation in the individual keograms are somewhat offset from each other.

The distinctive AO- Λ event visible in the boxes in both Figs. 5a and 5b keograms strongly suggests that Figs. 2 and 3 spread-F events are local manifestation of a mesoscale/hemispheric event. The keograms are not sufficient to explain the source of the mesoscale structure. Hence, the possible space weather aspect of the AO- Λ events and the underlying MLSpF activity caught our attention. Initial investigation of the magnetometer results showed a sudden drop in global SMR index (Fig. 6b) at the beginning of AO event (first red box of all relevant figures) leading to our examination of the parallel space weather and geomagnetic activity represented in Fig. 6. In Fig. 6, solar wind parameters, propagated to Earth from instruments at L1, are plotted on one-minute cadence over the same time interval (~22:30 — ~10:30 LT) as in Figs. 2 and 3. Also plotted is the SuperMAG SMR (ring current) index and the magnetic north geomagnetic field component from the HUA (Huancayo, Peru) and SJG (San Juan, Puerto Rico) magnetometers. The red boxes indicate the same event intervals as those in Figs. 2 and 3 while the centers of those two intervals are identified by the arrows in Fig. 5a keogram. Solar wind proton concentration is plotted vs. time in Fig. 6a. What appears to be the signature onset event, with proton concentration quickly dropping by 1/3rd, occurs at AO local midnight. This event is readily identified in magnetometer results of Fig. 6b as well as in Fig. 6c solar wind dynamic pressure, and Fig. 6d

solar wind magnetic field configuration. The AO F-region upwelling event occurs in the interval defined by the right-hand red box in Fig. 6 and, on the mesoscale, by the right-hand arrow in Fig. 5a keogram.

4. Discussion

The AO-local MLSpF event was observed by both the PIRI 4.42 MHz radar and the dual-beam ISRs and then identified in corresponding GNSS delta-vTEC observations as well as in the SuperMAG and OMNI datasets. The combined hybrid deep-wide-context wide-beam, low power HF radar and dual-beam, deep-context ISR results point a highly unstable local to near-mesoscale ionosphere. Keograms of the delta-vTEC data and comparison with appropriate SuperMAG and OMNI data supply critical wide-context for a more complete multi-scale picture of the event. Similar multi-instrument studies have been carried out by Miller et al. (1997) and Seker et al. (2008). From and Meehan (1988) reported observations of an MLSpF event observed with an HF radar. GNSS-TEC results are presented in the keogram format that was introduced by Eather et al. (1976). We adapt the keogram in the approach developed by Dinsmore et al. (2021a) with data processing procedures fully documented in Dinsmore et al. (2021b).

The multi-instrument data sets presented in this paper started with the PIRI HF radar and a prototype wave interaction experiment using the HF heating facility but evolved into a multi-instrument, multi-scale meta-instrument that, we propose, revealed an apparently local midlatitude spread-F event to be triggered by a modest shift in the solar wind properties. This effort was conducted during the March 2017 HF heating campaign at AO. The HF radar results (Fig. 2) suggest a highly unstable ionosphere with range-spread spread-F over the interval ~23:40 to 04:00 when the peak plasma frequency dropped below the 4.42 MHz radar frequency. The parallel two-beam ISR observations (Fig. 3) show a classic low geomagnetic activity, near solar minimum nighttime F-region with mild structure until a major upwelling event with embedded kilometer scale structure. As discussed in the introduction, these events have been attributed to local Perkins instabilities with

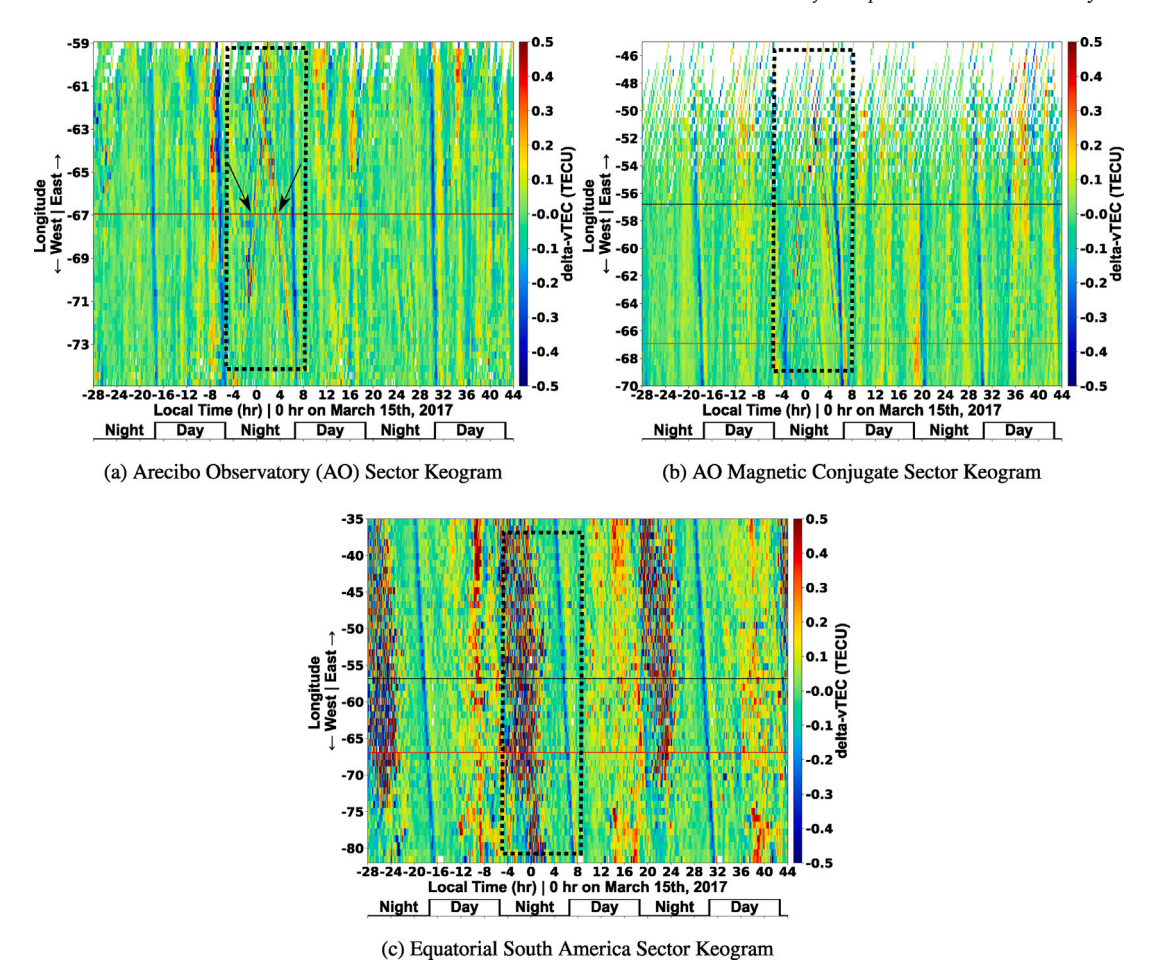


Fig. 5. Keograms corresponding to Fig. 4 averaging frameworks. (a) delta-vTEC keogram for the AO sector (Caribbean region) using the keogram Fig. 4a averaging-framework. In all panels the red horizontal line indicates the longitude of AO and the black horizontal line indicates the longitude of magnetic conjugate point of AO while the dotted black box indicates the full MLSpF-like event period revealed in Figs. 2 and 3. The inverted-V structure inside the boxes in panel A and B are referred to as AO-A throughout the text. The AO-A event begins at \sim 3 (21:00) h. and extends local surnise at \sim 06:30 h. Note that day/night transitions are visible as the near-vertical or somewhat diagonal stripes that coincide with AO-local day/night transitions shown in (b) below each keogram. The night-day transition is well defined while the day-night transition is much less o. Also note that the longitude range is much wider for panels (b) and (c) than for (a). The panel (a), (b), & (c) keograms incorporate \sim 3, \sim 9, & \sim 12 million data points, respectively.

the upwelling structure defined as mid-latitude spread-F. Together, the uniquely-sensitive, deep-context, two-(1/6th degree) beam AO ISR paired with the wide-context HF radar provided considerable insight into AO F-region over sub-kilometer to nearly mesoscale. As noted in the Introduction, Perkins-like instabilities, manifested as mid-latitude spread-F, have been both theoretically and experimentally considered to a local process. However, the HF radar results viewed relative to the ISR results suggest that an even wider context for the radar results is needed. This led to examination of the AO-sector GNSS delta-vTEC measurements in keogram form as shown in Fig. 5a which firmly establishes that the AO radar results are local manifestations of a mesoscale process. This process is expanded to nighttime hemispheric processes as revealed in the AO-conjugate-sector keogram shown in Fig. 5a which reveals approximately the same delta-vTEC structure as that shown in Fig. 5a. For sake of completeness the South America magnetic equatorial delta-vTEC keogram is also given (Fig. 5c). This shows strong delta-vTEC structuring, relative to the adjacent nights, over the AO observing period. We take this structuring to be evidence of equatorial spread-F (Kudeki et al., 2007) with some hint that the cause of the mid-latitude AO- Λ delta-vTEC structure also influenced the ESpF intensity.

Having established that the AO HF radar and ISR mid-latitude spread-F were a manifestation of at least a nighttime hemispheric process, we turned to examination of the relevant OMNI solar wind properties and SuperMAG magnetometer network data sets. Comparison of the data sets suggests that a modest change in the solar wind

pressure and B-field properties "launched" the events observed by radar and in the keograms. In combining (fusing) and comparing these diverse data sets we have created a meta-instrument spanning vast scales that seems to demonstrate the strongly coupled, systems-of-systems response of the global magnetosphere-ionosphere system to a modest space weather event. Next, we discuss each dataset in somewhat greater detail.

4.1. PIRI HF RADAR observations

The PIRI observations, shown in RTI (Range, Time, Intensity) format in Fig. 2, began at 23:41 AST, 14 March 2017 and continue until 11:15 AST, 15 March 2017. Instrument details are given in Section 2.1. The HF radar can be thought of as a single frequency ionosonde. It reveals pronounced range-spread spread-F (a wide spread in range of >600 km) over the 23:41 - ~04:00 LT interval after which the ionosphere peak plasma frequency drops below the 4.42 MHz radar frequency resulting in no ionospheric signal returns until photochemical sunrise at ~06:50 AST. In general, such range spreading is attributed to scattering from F-region structures at some significant horizontal distance from the radar zenith location. The radio science of the ionospheric signals is important as diffuse scattering from relatively small overdense plasma "blobs" dominate during the night hours and classical ordinary/extraordinary mode Fresnel area reflections appear at sunrise. That is, the nighttime F-region is in some sense unstable the whole

night in that it appears to be highly structured on scales approaching the radar wavelength ($\lambda_{piri}=68$ m). The Fig. 2 RTI plots suggest that between 23:40 LT and 04:00 LT a series of at least 9 "structures" appear at greater range and appear to approach the radar. The upwelling event, that stands out in Fig. 3 ISR results, is somewhat distinctive here too. The ISR results reveal that this particular structure is in fact at a higher altitude than the surrounding ionosphere. This event region is contained within the right-hand box in all relevant figures.

Although the HF heater was running in pulsed mode over the entire nighttime interval, possible ionospheric effects of the heater, e.g., causing ambiguous HF radar echoes due to electron gas heating, are not expected, or detected. This conclusion is reached in part due to available ionograms from the nearby ionosonde at Ramey, Puerto Rico (18.5°N, 67.1°W), located 25 miles northwest of AO. The 20-minute cadence ionograms, included as ancillary data (Fig. A.1), indicate that the critical frequency of the F-region was well below the operational heating frequency at least until 06:00 LT implying that the HF radar observations, beyond interference, were not influenced by the heater. The ionograms do show ongoing, near solar minimum, low geomagnetic activity (Kp~2) spread-F.

4.2. 430 MHz ISR observations

The dual, narrow-beam 430 MHz AO ISR (see Fig. 1) was in operation over the 14/15 March 2017 observing period in support of the originally-proposed wave interaction experiment described earlier. The resulting RTI plots are given in Fig. 3. These Deep-Context ISR observations reveal an ionosphere upwelling event (right-hand box) with km-scale substructure. It is this event and the corresponding event seen in the HF radar results that attracted our initial interest and led us to consider the less obvious event in the left-hand box. Upwelling events are relatively common in AO nighttime ISR observations and are usually attributed to local Perkins-like instabilities possibly initiated by one of a variety of suspect "triggers" such as Acoustic Gravity Waves (AGWs) (Mathews et al., 2001a). However, the HF radar results reveal that the "background" ionosphere is significantly structured over the entire observing period suggesting that an environment supporting Perkins-like instabilities may have been present the whole time. Notice that the ~04:00-07:00 LT region with no ionospheric HF radar returns in Fig. 2 is clearly visible in Fig. 3 ISR results.

In contrast to the ongoing HF radar range-spread returns, the ISR RTI plots show a somewhat featureless ionosphere over the period between the two events indicated by the boxes. It must be remembered that the ISR beams are very narrow enabling direct imaging of structure down to the kilometer scale (Mathews et al., 2001a). For example, the structure within the upwelling feature is, not surprisingly, different within the two beams confirming that the structuring is B-field aligned. Contrasting the rather calm ionosphere in the narrow-beam ISR data with the apparently "turbulent structure" ionosphere visible in the wide-beam HF radar data indicates both large scale—approaching mesoscale—likely moving structures made visible by HF scattering from many small-scale structures (Mathews, 2004). The combination of the HF radar and ISR results suggest that the mesoscale ionospheric structure should be examined. Fortunately, the GNSS/GPS receiver network in the AO-sector is sufficiently dense to yield the required results.

4.3. GNSS delta-vTEC measurements

While GNSS-TEC measurements lack radar-like range resolution, a sufficiently distributed and dense receiver ensemble provides, in principle, a movie-like view of the ionosphere TEC (Total Electron Content) on scales ranging from a few 10's kilometers to the mesoscale and beyond. Interpretation of individual measurements relies on the assumption that most of the TEC lies within the electron-dense F-region which we take to be centered at 350 km. In particular, the geographical

location of individual, 30 s average TEC measurements is taken to be the 350 km altitude pierce-point on the receiver-satellite ray path at the sample time. For our purposes, the F-region sensitivity makes GNSS-TEC viable for establishing the mesoscale context of mid-latitude spread-F (MLSpF) and equatorial spread-F (ESpF). As described in Section 2.4, we use delta-vTEC activity as an indicator of general F-region disturbance structures including spread-F as observed by ISR. Given the marginal area coverage of GNSS-TEC receivers in the AO-sector (and the difficulty of interpreting movies) we present the delta-vTEC results in keogram form per Section 2.4. These keograms are given in Fig. 5. Millions of individual measurements are required for each keogram.

The Arecibo-sector keogram (Fig. 5a) places the ISR upwelling event (right hand box, Figs. 2 and 3) in a much wider and intriguing context. The upwelling event keogram location is indicated by the right-hand arrow. The Figs. 2 and 3 left-hand-box event is indicated by Fig. 5a left-hand arrow. The (unexpected) AO- Λ structure in Fig. 5a is a time/longitude region of enhanced delta-vTEC disturbance that began to the west $(-71^{\circ} \text{ longitude})$ of AO at \sim -3 h $(\sim 21:00, 14 \text{ March } 17)$ and appeared to propagate eastward arriving at AO at about the time, 0 h, indicated by the lefthand arrow. The disturbance continued to the east where it merged with another disturbance region that had started somewhat earlier. The disturbance region then appeared to propagate westward passing over AO at the time of the upwelling event indicated by the left-hand arrow. The disturbance continues westward until the night-to-day transition (photo-chemical sunrise) dissipates it at -75° longitude. The delta-vTEC disturbance apparent propagation speed is \sim 300 km/h (\sim 85 m/s). The noisy region at the top of the keogram is due to lack of receivers (and islands) to the east of AO. In comparing the wide-context delta-vTEC activity during the nights before and after the observation night, it is clear that F-region disturbance activity was relatively enhanced on the night of 14/15 March 2017 and that it was this activity observed at AO with the deep-context radars.

The overall spread-F event observed with PIRI, the AO ISR, and GNSS-TEC is non-local and occurs within the latitude range visible to Puerto Rico and Hispaniola ($\sim 17^{\circ}$ to $\sim 22^{\circ}$ latitude). The event covers -61° to -75° longitude and activity likely extends over the Atlantic Ocean to the east. The Fig. 5a keogram AO- Λ event appears to propagate in longitude (for both directions) and lasts from ~ -3 to +6.5 h. The perpendicular keogram (latitudinal slicing) shows no propagation perhaps because the latitude coverage is small. A concentrated "bubble" of activity at ~ 2 LT between 20° to 21° latitudes corresponds to the muddled activity seen in Fig. 5a at around -62° longitude.

To better gauge the electrodynamics leading to Fig. 5a AO- Λ structure, we turn to the AO-magnetic-conjugate (\sim 58° W, \sim 37° S at Fregion heights) sector keogram given in Fig. 5b. The conjugate keogram exhibits a similar longitudinally-only propagating AO- Λ feature during the same time interval as in the AO-sector. The later westward feature reaches the night-to-day terminator somewhat before it appears to reach AO longitude. Note that the conjugate keogram reaches far to the geographic east relative to the AO keogram while not extending as far to the west. Thus, the mapping of the AO- and AO-conjugate AO- Λ feature is not perfect. Still, it seems clear that electrodynamic mapping of this feature, as expected for the unshorted, highly-conducting magnetic flux tubes, is present over the \sim -3 to +6.5 AST lifetime of the AO- Λ event.

Finally, we examine the geomagnetic equator region keogram (Fig. 5c) for sake of completeness. This keogram spans the widest longitude coverage of the three keograms and again note that the day-night indicator corresponds to AO. Strong delta-vTEC disturbance occurs east of about 72° longitude during each night of the three nights presented. We assume that the disturbance region is due largely to equatorial spread-F (ESpF) but caution that the nighttime E-region electrojet may contribute. Due to strong ESpF signature each night it is difficult to conclude any relationship with the AO- Λ structure in the first two keograms. However, we do note that at 00:00 LT a disturbance feature appears west of 72° longitude. This feature is not present during the other two nights. We intend to build a delta-vTEC keogram climatology of this sector that may ultimately help understanding of ESpF and its response to space weather events.

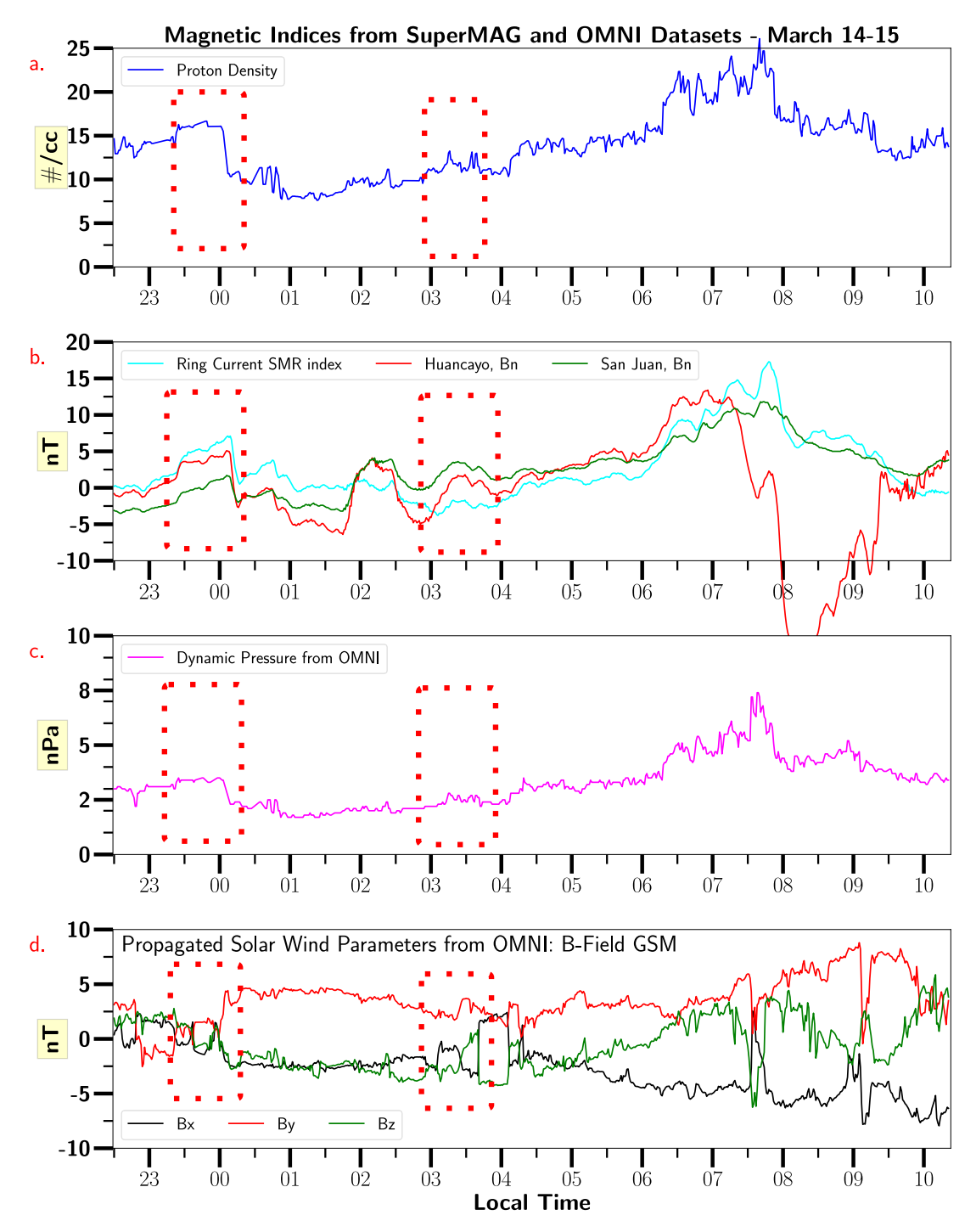


Fig. 6. Relevant SuperMAG and OMNI data that ties the mesoscale event to the solar wind variations. The time span here corresponds to that of Figs. 2 and 3 with the boxed-in areas matching over all three figures. The left box includes the solar wind pressure pulse while both box areas highlight IMF realignment. Time extended versions of this figure are given as ancillary Figures A2 and A3. Figure A2 encompasses the entire AO-Λ event including the onset. Figure A3 includes the 12 h before Figure A2 and highlights all Bz-south regions.

4.4. SuperMAG and OMNI measurements

The Fig. 5a AO-sector keogram firmly ties the 4.42 MHz PIRI radar and dual-beam 430 MHz ISR results to the mesoscale delta-vTEC AO- Λ structure that begins at \sim -3 h, before radar coverage commences, and evolves over the nighttime hours. Further, the AO-conjugate sector keogram approximately mirrors the AO-sector keogram while the South American geomagnetic equator sector keogram mildly suggests some activity tied to that in the other sectors. To further understand the event in question we looked at the SuperMAG Ring current index (SMR),

the Huancayo (HUA) and San Juan (SJG) magnetometer data, and the corresponding OMNI solar wind data. Relevant data sets, plotted on the same time interval as Figs. 2 and 3, are given in Fig. 6. The solar wind parameters are time-wise propagated to the approximate magnetopause location.

The Fig. 6 red-dashed boxes correspond to the same boxes in Figs. 2 and 3. As seen in Fig. 6a proton concentration plot, the initial ISR-visible event (Fig. 3, left-hand box) corresponds to a slight jump in proton concentration followed by a rapid 30% drop. The dynamic pressure also exhibits a modest pressure pulse and the solar wind

magnetic field configuration shifts from all components slightly positive to Bz and Bx negative and By firmly positive. This event corresponds to the lefthand arrow in Fig. 5a. The SMR index and HUA/SJG Bn components all clearly "map" the solar wind event. We suggest that this solar wind event translates with little delay to the magnetometer response and to the AO F-region as imaged in the deep-context ISR results. As Fig. 5a AO-sector delta-vTEC keogram and radar results appear to be highly correlated (two arrows, Fig. 5a), we also conclude that the mesoscale ionospheric activity represented in the keograms is a response to the solar wind activity.

The F-region upwelling event (right hand boxes in Figs. 2, 3, 6) is easily identified in Fig. 3 ISR results and appears to be associated with the mesoscale delta-vTEC activity in Fig. 5a (right-hand arrow). Through electrodynamic mapping across the highly conducting magnetic flux tubes (with no shorting of the flux tubes in the respective E-regions) from AO to the AO conjugate region, the two opposite hemisphere sector F-regions are closely coupled. The relationship between solar wind events and the upwelling event appears to be most apparent in the solar wind magnetic field reconfiguration on the 03:00–04:00 LT interval as well in the HUA and SJG magnetometer results. The 01:45–02:45 LT HUA/SJG positive excursion seems to be in some sense local in that it does not correspond to a solar wind feature.

5. Conclusions

Using five diverse data sets, we demonstrate that apparently local ionospheric spread-F activity, observed with an HF radar and the Arecibo Observatory (AO) Incoherent Scatter Radars (ISR) under geomagnetically quiet conditions, is likely the local manifestation of a mesoscale or larger ionospheric response to relatively weak solar wind activity that included a weak pressure pulse and Interplanetary Magnetic Field (IMF) realignment events as revealed in the OMNI dataset. The ISR event (Fig. 3, right hand box) appears to be "classical" local spread-F often attributed to Perkins-like plasma instabilities, while the HF radar reveals large ionospheric structures coincident with the ISR event (Fig. 2). The AO spread-F activity is also apparent in the corresponding AO-sector GNSS delta-vTEC keogram (Fig. 5; Section 4.3) as well as in the superMAG and OMNI datasets (Fig. 6, Fig. A2, A3). The Fig. 6 OMNI data reveals solar wind structure that appears to correspond to the entire "AO- Λ " delta-vTEC keogram structure with little time delay. In particular, Fig. 6, left-box solar wind pressure pulse is evident in the superMAG SMR (ring current) index as well as in the HUA (Huancayo, Peru) and SJG (San Juan, Puerto Rico) magnetometer results. It is also evident in the ISR results. The delta-vTEC keograms and parallel superMAG and OMNI data supply a critical, and perhaps unique, wide-context yielding a more complete multiscale picture of the spread-F event observed in the deep-context radar results that, for example, reveal substructure as small as \sim 1 km. Similar multi-instrument studies have been carried out by Miller et al. (1997) and Seker et al. (2008). From and Meehan (1988) reported observations of an MLSpF event observed with an HF radar.

Observationally, the AO-local spread-F activity appears to be embedded within a mesoscale delta-vTEC (AO-A) feature revealed in both the AO-sector (Fig. 5a) and conjugate-AO-sector (Fig. 5b) keograms. The corresponding South America magnetic equator sector keogram (Fig. 5c) also hints at a parallel response. Examination of OMNI solar wind parameters, SMR, and the SJG and HUA individual magnetometer responses (Figs. 5 and A.2) all point to a likely association with the solar wind properties over an 11-hour AO keogram nighttime interval (Fig. A2). The rapid response of the nightside AO- and AO-conjugate sector ionospheres to the solar wind activity suggests an ionospheric response to prompt penetration electric fields (PPEF; e.g., Hashimoto et al., 2020 & references therein). While PPEFs have been suggested only during geomagnetic storms, PPEFs seem to be an appropriate mechanism here particularly if associated with partial ring current

generation (e.g., Fukushima and Kamide, 1973). This even though the generative solar wind event is, relatively, quite weak.

To extend this conjecture, the system-of-systems mechanism invoked in Hashimoto et al. (2020) is that of a solar wind event enhancing, perhaps via partial ring current features, Region 1 FAC (Field-Aligned or Birkland Currents) in the magnetosphere cusp region with the FAC electrodynamic closure in the ionosphere (Pederson currents) forming an "antenna" that launches TM_0 (Transverse Magnetic mode 0) electromagnetic (EM) waves into the earth-ionosphere waveguide (transmission line) along which the waves propagate to lower latitudes at the waveguide speed of light. Thus, a fraction of the solar wind energy transferred into the magnetospheric cusp region arrives with little delay at low latitudes where it is manifested as the PPEF (Kikuchi, 2014) action on the, in our case, nighttime ionosphere. We additionally conjecture that the nighttime earth-(lower)ionosphere waveguide (transmission line) properties are ideal, relative to daytime, for efficient transmission of PPEF. This as the lossy ionospheric D-region is absent and the E-region is largely electrodynamically decoupled from the

To conclude, "local" nighttime ionospheric spread-F activity at AO appears to be embedded within a mesoscale delta-vTEC keogram feature that is likely associated with a small space weather event that involves solar wind pressure and B-field realignment activity over an ~8-hour interval. The combination of deep-context radar results and wide-context delta-vTEC results suggests a complex, electrodynamic system-of-systems, magnetospheric-ionospheric response to the relatively small solar wind feature impacting the dayside magnetosphere. Assuming a relatively high rate of "small" solar wind features resulting in PPEF action at low latitudes, the net space weather energy input to the low-latitude nighttime ionosphere is likely significant. In any case, the need to examine magnetosphere ionosphere coupling across a wide range of scales with deep-context ISR and HF radar and widecontext GNSS-TEC, superMAG, and OMNI datasets is shown. The AO ISR, a major component of the meta-instrument employed in this study, was critical to this analysis. It is imperative that our society makes a concerted effort in bringing AO-like facilities forward as space weather becomes of growing importance to human infrastructure both on the Earth and beyond the Earth.

Declaration of competing interest

The authors declare that they have no known competing financial interests or personal relationships that could have appeared to influence the work reported in this paper.

Data availability

Data will be made available on request.

Acknowledgments

This work partially supported by a National Science Foundation grant AGS 1241407 to The Pennsylvania State University, USA. We thank PI Anthea Coster for the Madrigal TEC data and PI César Valladares for Low-Latitude Ionospheric Sensor Network (LISN) TEC data. Data for the TEC processing is provided from the following organizations: UNAVCO, Scripps Orbit and Permanent Array Center, Institut Geographique National, France, International GNSS Service, The Crustal Dynamics Data Information System (CDDIS), National Geodetic Survey, Instituto Brasileiro de Geografia e Estatística, RAMSAC CORS of Instituto Geográfico Nacional de la República Argentina, Arecibo Observatory, Low-Latitude Ionospheric Sensor Network (LISN), Topcon Positioning Systems, Inc., Canadian High Arctic Ionospheric Network, Institute of Geology and Geophysics, Chinese Academy of Sciences, China Meteorology Administration, Centro di Ricerche Sismologiche, Système d'Observation du Niveau des Eaux Littorales (SONEL), RENAG

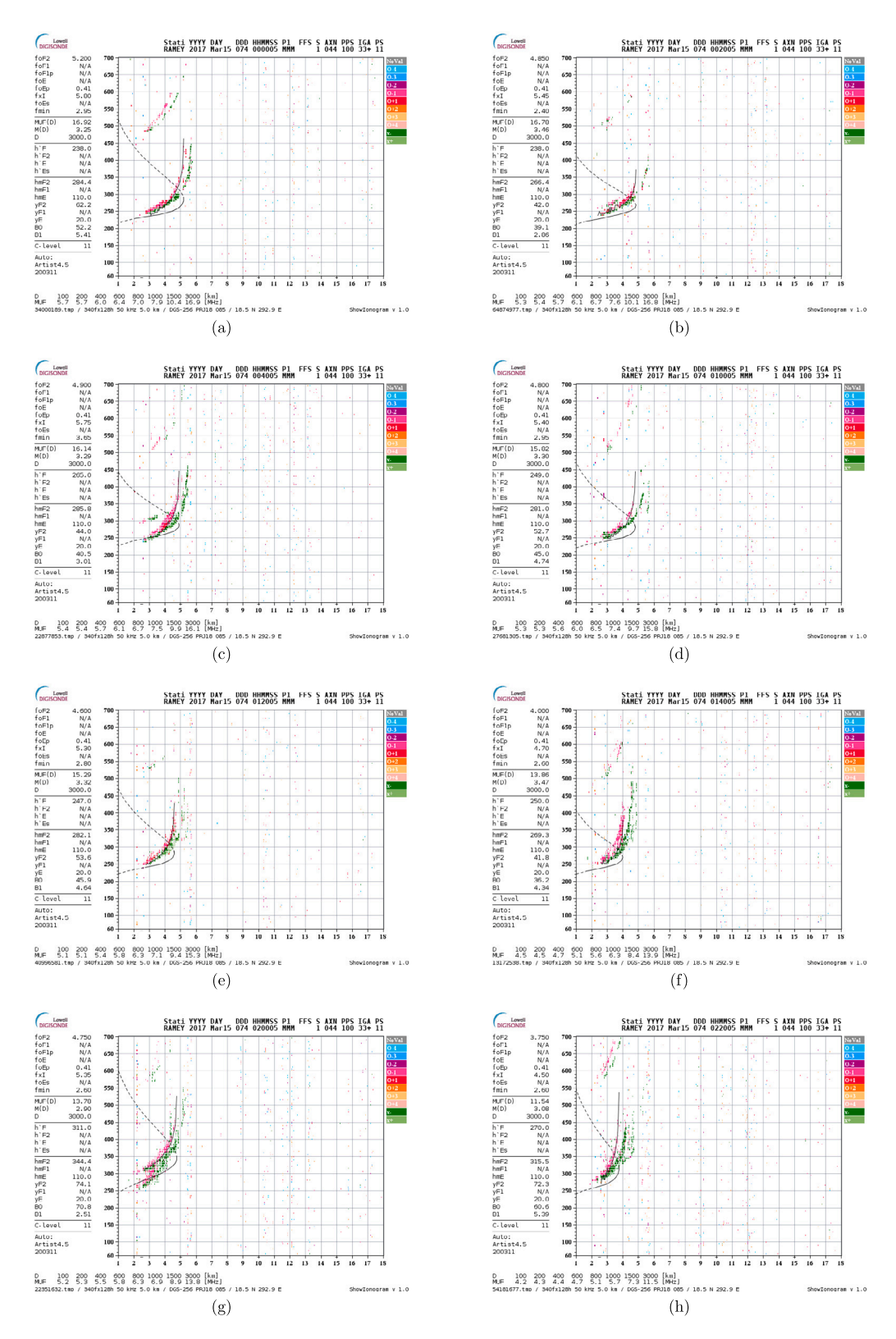


Fig. A.1. 20-min cadence ionograms from ionosonde located at Ramey. Classical spread-F is apparent through the whole set. The ionograms are taken from: http://ramey.ionosonde.net.

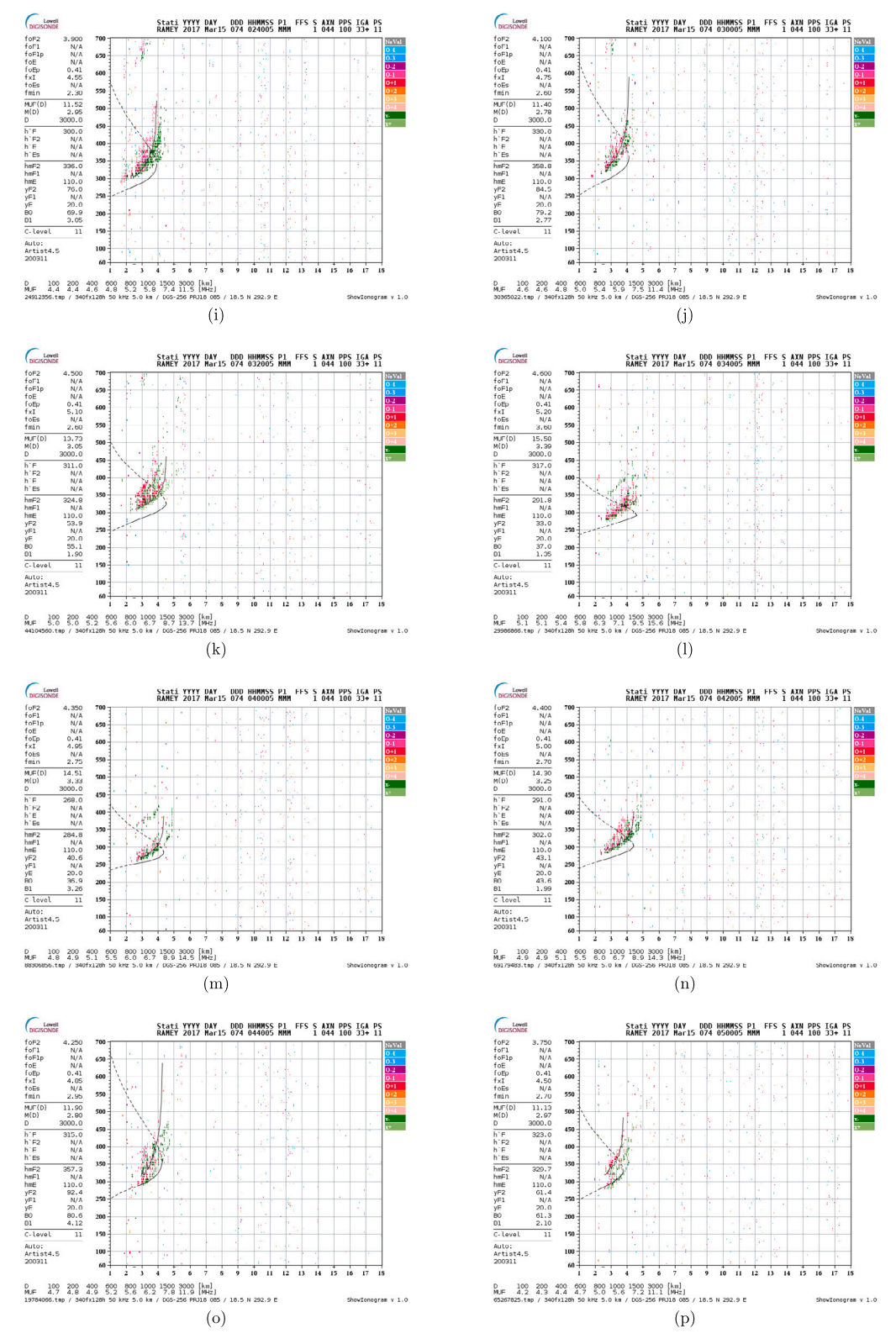


Fig. A.1. (continued).

: REseau NAtional GPS permanent, GeoNet - the official source of geological hazard information for New Zealand, GNSS Reference Networks, Finnish Meteorological Institute, SWEPOS - Sweden, Hartebeesthoek Radio Astronomy Observatory, Crustal Dynamics Data Information System (CDDIS), Astronomical Institute of the University of Bern, TrigNet Web Application, South Africa, Australian Space Weather Services, RETE INTEGRATA NAZIONALE GPS, Estonian Land Board, and Virginia

Tech Center for Space Science and Engineering Research. The Low Latitude Ionospheric Sensor Network (LISN) is a project led by the University of Texas at Dallas in collaboration with the Geophysical Institute of Peru and other institutions that provide information to benefit the space weather scientific community. For the ground magnetometer data we gratefully acknowledge: INTERMAGNET, Alan Thomson; CARISMA, PI Ian Mann; CANMOS, Geomagnetism Unit of the Geological Survey

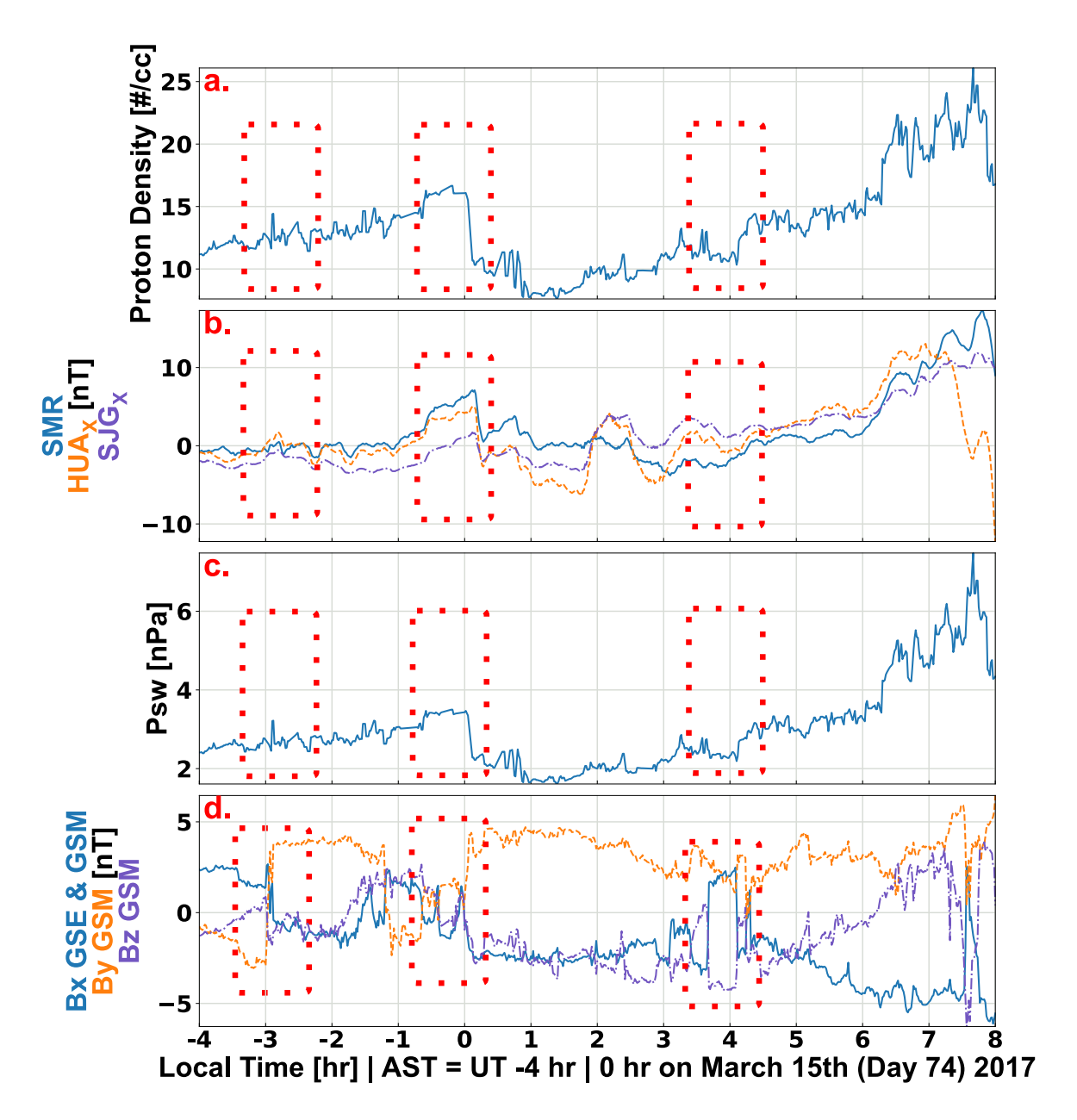


Fig. A.2. Red dashed lines that are present near the solar wind the pressure pulse and B-field reconfiguration events, are corresponding to the dashed boxes from Figs. 2, 3 and 5a. First red box shows the starting point of the inverted-V event that spans between — 04:00 to 07:00 Atlantic Standard Time from the Fig. 5a keogram.

of Canada; The S-RAMP Database, PI K. Yumoto and Dr. K. Shiokawa; The SPIDR database; AARI, PI Oleg Troshichev; The MACCS program, PI M. Engebretson; GIMA; MEASURE, UCLA IGPP and Florida Institute of Technology; SAMBA, PI Eftyhia Zesta; 210 Chain, PI K. Yumoto; SAMNET, PI Farideh Honary; IMAGE, PI Liisa Juusola; Finnish Meteorological Institute, PI Liisa Juusola; Sodankylä Geophysical Observatory, PI Tero Raita; UiT the Arctic University of Norway, TromsøGeophysical Observatory, PI Magnar G. Johnsen; GFZ German Research Centre For Geosciences, PI Jürgen Matzka; Institute of Geophysics, Polish Academy of Sciences, PI Anne Neska and Jan Reda; Polar Geophysical Institute, PI Alexander Yahnin and Yarolav Sakharov; Geological Survey of Sweden, PI Gerhard Schwarz; Swedish Institute of Space Physics, PI Masatoshi Yamauchi; AUTUMN, PI Martin Connors; DTU Space, Thom Edwards and PI Anna Willer; South Pole and McMurdo Magnetometer, PI's Louis J. Lanzarotti and Alan T. Weatherwax; ICESTAR; RAPIDMAG; British Artarctic Survey; McMac, PI Dr. Peter Chi; BGS, PI Dr. Susan

Macmillan; Pushkov Institute of Terrestrial Magnetism, Ionosphere and Radio Wave Propagation (IZMIRAN); MFGI, PI B. Heilig; Institute of Geophysics, Polish Academy of Sciences, PI Anne Neska and Jan Reda; University of L'Aquila, PI M. Vellante; BCMT, V. Lesur and A. Chambodut; Data obtained in cooperation with Geoscience Australia, PI Andrew Lewis; AALPIP, co-PIs Bob Clauer and Michael Hartinger; MagStar, PI Jennifer Gannon; SuperMAG, PI Jesper W. Gjerloev; Data obtained in cooperation with the Australian Bureau of Meteorology, PI Richard Marshall. We additionally thank NASA's Space Physics Data Facility in Goddard Space Flight Center for the OMNIWeb service that provided OMNI data (https://omniweb.gsfc.nasa.gov/ow_min.html)

Appendix

See Figs. A.1-A.3.

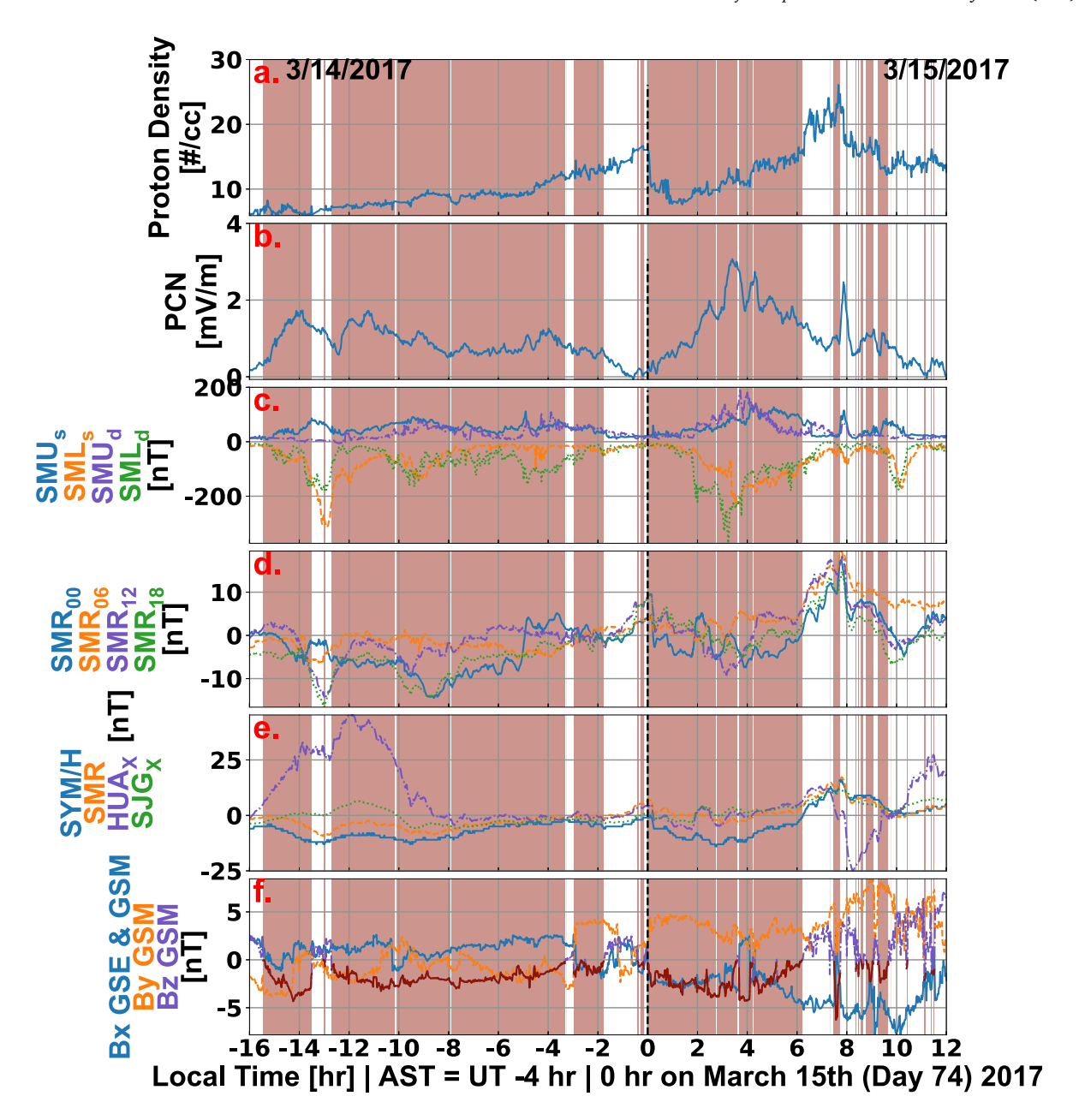


Fig. A.3. This figure is an extended version of Fig. A.2 which starts 12 hours before Fig. A.2 and highlights all Bz-south regions.

References

Behnke, R., 1979. F layer height bands in the nocturnal ionosphere over Arecibo. J. Geophys. Res. Space Phys. 84 (A3), 974–978.

Berkner, L., Wells, H., 1934. F-region ionosphere-investigations at low latitudes. Terr. Magn. Atmos. Electr. 39 (3), 215–230.

Booker, H.G., 1961. A local reduction of F-region ionization due to missile transit. J. Geophys. Res. 66 (4), 1073–1079.

Booker, H., Wells, H., 1938. Scattering of radio waves by the F-region of the ionosphere. Terr. Magn. Atmos. Electr. 43 (3), 249–256.

Bostan, S.M., 2018. The Discovery of Novel Ionospheric Phenomenon Using a Software-Defined High Frequency Radar (Ph.D. thesis). Electrical Engineering, The Pennsylvania State University.

Bostan, S.M., Urbina, J.V., Mathews, J.D., Bilén, S.G., Breakall, J.K., 2019. An HF software-defined radar to study the ionosphere. Radio Sci. 54 (9), 839–849.

Bowman, G., 1990. A review of some recent work on mid-latitude spread-F occurrence as detected by ionosondes. J. Geomagn. Geoelectr. 42 (2), 109–138.

Coster, A., Buonsanto, M., Gaposchkin, E., Tetenbaum, D., Thornton, L., 1990. Ionospheric and tropospheric path delay obtained from GPS integrated phase, incoherent scatter and refractometer data and from IRI-86. Adv. Space Res. 10 (8), 105–108. Coster, A.J., Gaposchkin, E.M., Thornton, L.E., 1992. Real-time ionospheric monitoring system using GPS. Navigation 39 (2), 191–204.

Coster, A., Williams, J., Weatherwax, A., Rideout, W., Herne, D., 2013. Accuracy of GPS total electron content: GPS receiver bias temperature dependence. Radio Sci. 48 (2), 190–196.

Dinsmore, R.L., 2021. GRITI: General resource for ionospheric transient investigations. URL https://github.com/dinsmoro/GRITI. (Latest version: January 12, 2021).

Dinsmore, R., Mathews, J., Coster, A., Robinson, R., Sarkhel, S., Erickson, P.J., Urbina, J., 2021a. Multi-instrument observations of SCIPS: 1. ISR and GPS TEC results. J. Atmos. Sol.-Terr. Phys. 213, 105515.

Dinsmore, R., Mathews, J.D., Urbina, J., 2021b. General resource for ionospheric transient investigations (GRITI): An open-source code developed in support of the Dinsmore others, (2021) results. MethodsX 8, 101456.

Eather, R., Mende, S., Judge, R., 1976. Plasma injection at synchronous orbit and spatial and temporal auroral morphology. J. Geophys. Res. 81 (16), 2805–2824.

Evans, J., 1972. Ionospheric movements measured by incoherent scatter: A review. J. Atmos. Terr. Phys. 34 (2), 175–209.

From, W., Meehan, D., 1988. Mid-latitude Spread-F structure. J. Atmos. Terr. Phys. 50 (7), 629–638. http://dx.doi.org/10.1016/0021-9169(88)90061-x.

Fukao, S., Kelley, M.C., Shirakawa, T., Takami, T., Yamamoto, M., Tsuda, T., Kato, S., 1991. Turbulent upwelling of the mid-latitude ionosphere: 1. Observational results by the MU radar. J. Geophys. Res. Space Phys. 96 (A3), 3725–3746.

- Fukushima, N., Kamide, Y., 1973. Partial ring current models for worldwide geomagnetic disturbances. Rev. Geophys. 11 (4), 795–853.
- Gjerloev, J., 2009. A global ground-based magnetometer initiative. EOS Trans. Am. Geophys. Union 90 (27), 230–231.
- Hashimoto, K.K., Kikuchi, T., Tomizawa, I., Hosokawa, K., Chum, J., Buresova, D., Nose, M., Koga, K., 2020. Penetration electric fields observed at middle and low latitudes during the 22 June 2015 geomagnetic storm. Earth, Planets Space 72 (1), 1–15.
- Herman, J.R., 1966. Spread f and ionospheric F-region irregularities. Rev. Geophys. 4 (2), 255–299.
- Huang, C.-S., 2020. Systematical analyses of global ionospheric disturbance current systems caused by multiple processes: Penetration electric fields, solar wind pressure impulses, magnetospheric substorms, and ULF waves. J. Geophys. Res. Space Phys. 125 (9), e2020JA027942.
- Hysell, D., Larsen, M., Fritts, D., Laughman, B., Sulzer, M., 2018. Major upwelling and overturning in the mid-latitude F region ionosphere. Nature Commun. 9 (1), 1–11.
- Kelley, M.C., 2009. The Earth's Ionosphere: Plasma Physics and Electrodynamics. Academic Press.
- Kelley, M.C., Fukao, S., 1991. Turbulent upwelling of the mid-latitude ionosphere: 2. Theoretical framework. J. Geophys. Res. Space Phys. 96 (A3), 3747–3753.
- Kesaraju, S., Mathews, J., Milla, M., Vierinen, J., 2017. Range-Doppler mapping of space-based targets using the JRO 50 MHz radar. Earth, Moon, Plan. 120 (3), 169–188. http://dx.doi.org/10.1007/s11038-017-9510-0.
- Keskinen, M.J., Ossakow, S., 1983. Theories of high-latitude ionospheric irregularities: A review. Radio Sci. 18 (06), 1077–1091.
- Kikuchi, T., 2014. Transmission line model for the near-instantaneous transmission of the ionospheric electric field and currents to the equator. J. Geophys. Res. Space Phys. 119 (2), 1131–1156.
- Kudeki, E., Akgiray, A., Milla, M., Chau, J.L., Hysell, D.L., 2007. Equatorial spread-F initiation: Post-sunset vortex, thermospheric winds, gravity waves. J. Atmos. Sol.-Terr. Phys. 69 (17–18), 2416–2427.
- Lehtinen, M., Damtie, B., Nygrén, T., 2004. Optimal binary phase codes and sidelobe-free decoding filters with application to incoherent scatter radar. Ann. Geophys. 22 (5), 1623–1632. http://dx.doi.org/10.5194/angeo-22-1623-2004.
- Mathews, J., 1984. The incoherent scatter radar as a tool for studying the ionospheric D-region. J. Atmos. Terr. Phys. 46 (11), 975–986.
- Mathews, J.D., 1986. Incoherent scatter radar probing of the 60-100-km atmosphere and ionosphere. IEEE Trans. Geosci. Remote Sens. (5), 765–776.
- Mathews, J., 2004. Radio science issues surrounding HF/VHF/UHF radar meteor studies. J. Atmos. Sol.-Terr. Phys. 66 (3–4), 285–299.
- Mathews, J., 2013a. Fifty years of Radio Science at Arecibo Observatory: A brief overview. URSI Radio Sci. Bull. 2013 (346), 12–16.
- Mathews, J., 2013b. A short history of geophysical radar at Arecibo Observatory. Hist. Geo- Space Sci. 4 (1), 19–33.
- Mathews, J., Gonzalez, S., Sulzer, M., Zhou, Q.-H., Urbina, J., Kudeki, E., Franke, S., 2001a. Kilometer-scale layered structures inside Spread-F. Geophys. Res. Lett. 28 (22), 4167–4170. http://dx.doi.org/10.1029/2001gl013077.
- Mathews, J., Harper, R., 1972. Incoherent scatter radar observations of spread-F producing ionospheric structures at Arecibo. J. Atmos. Terr. Phys. 34 (6), 1119–1127.

- Mathews, J., Machuga, D., Zhou, Q., 2001b. Evidence for electrodynamic linkages between Spread-F, ion rain, the intermediate layer, and sporadic E: results from observations and simulations. J. Atmos. Sol.-Terr. Phys. 63 (14), 1529–1543. http://dx.doi.org/10.1016/s1364-6826(01)00034-7.
- Miller, C.A., Swartz, W., Kelley, M., Mendillo, M., Nottingham, D., Scali, J., Reinisch, B., 1997. Electrodynamics of midlatitude spread F: 1. Observations of unstable, gravity wave-induced ionospheric electric fields at tropical latitudes. J. Geophys. Res. Space Phys. 102 (A6), 11521–11532.
- Ossakow, S.L., 1981. Spread-F theories—A review. J. Atmos. Terr. Phys. 43 (5-6), 437-452.
- Perkins, F., 1973. Spread F and ionospheric currents. J. Geophys. Res. 78 (1), 218–226.Rideout, W., Coster, A., 2006. Automated GPS processing for global total electron content data. GPS Solut. 10 (3), 219–228.
- Seal, R., 2012. GNURADAR version: 3.0.0. URL https://github.com/rseal/GnuRadar. Latest version: Aug 22, 2012.
- Seal, R., 2017. Bit pattern generator software v-2.0. URL https://github.com/rseal/ BitPatternGenerator. Latest version: February 23, 2017.
- Seker, I., Livneh, D.J., Makela, J.J., Mathews, J.D., 2008. Tracking F-region plasma depletion bands using GPS-TEC, incoherent scatter radar, and all-sky imaging at Arecibo. Earth Planets Space 60 (6), 633–646.
- Seker, I., Mathews, J.D., Wiig, J., Gutierrez, P.F., Friedman, J.S., Tepley, C.A., 2007.
 First results from the Penn state allsky imager at the Arecibo observatory. Earth Planets Space 59 (3), 165–176.
- Sulzer, M., Mathews, J.D., Tomko, A., 1982. A UHF cross-modulation D region heating experiment with aeronomic implications. Radio Sci. 17 (2), 435–443.
- SuperMAG, 2022. SuperMAG: Global magnetic field observations and products made possible by the contributors. URL https://supermag.jhuapl.edu/. (Accessed 9 April 2022).
- Swartz, W.E., Kelley, M.C., Makela, J.J., Collins, S.C., Kudeki, E., Franke, S., Urbina, J., Aponte, N., Sulzer, M.P., González, S.A., 2000. Coherent and incoherent scatter radar observations during intense mid-latitude spread F. Geophys. Res. Lett. 27 (18), 2829–2832.
- Tsurutani, B., Mannucci, A., Iijima, B., Abdu, M.A., Sobral, J.H.A., Gonzalez, W., Guarnieri, F., Tsuda, T., Saito, A., Yumoto, K., et al., 2004. Global dayside ionospheric uplift and enhancement associated with interplanetary electric fields. J. Geophys. Res. Space Phys. 109 (A8).
- Tsurutani, B., Verkhoglyadova, O., Mannucci, A., Saito, A., Araki, T., Yumoto, K., Tsuda, T., Abdu, M., Sobral, J., Gonzalez, W.D., et al., 2008. Prompt penetration electric fields (PPEFs) and their ionospheric effects during the great magnetic storm of 30–31 October 2003. J. Geophys. Res. Space Phys. 113 (A5).
- Vierinen, J., Coster, A.J., Rideout, W.C., Erickson, P.J., Norberg, J., 2016. Statistical framework for estimating GNSS bias. Atmos. Meas. Tech. 9 (3), 1303–1312.
- Woodman, R., 2009. Spread F-an old equatorial aeronomy problem finally resolved? Ann. Geophys. 27 (5), 1915–1934.
- Zhou, Q., Mathews, J.D., Miller, C.A., Seker, I., 2006. The evolution of nighttime midlatitude mesoscale F-region structures: A case study utilizing numerical solution of the ns instability equations. Planet. Space Sci. 54 (7), 710–718.